Journal Pre-proof

Porosity Matters: Exploring its Impact on the Unlubricated Tribological Behavior of Copper

Roxane Lung, Karl Günter Schell, Christian Greiner

PII: S2666-8459(26)00205-9

DOI: https://doi.org/10.1016/j.rsurfi.2026.100913

Reference: RSURFI 100913

To appear in: *Results in Surfaces and Interfaces*

Received Date: 14 October 2025

Revised Date: 28 June 2026

Accepted Date: 30 July 2026

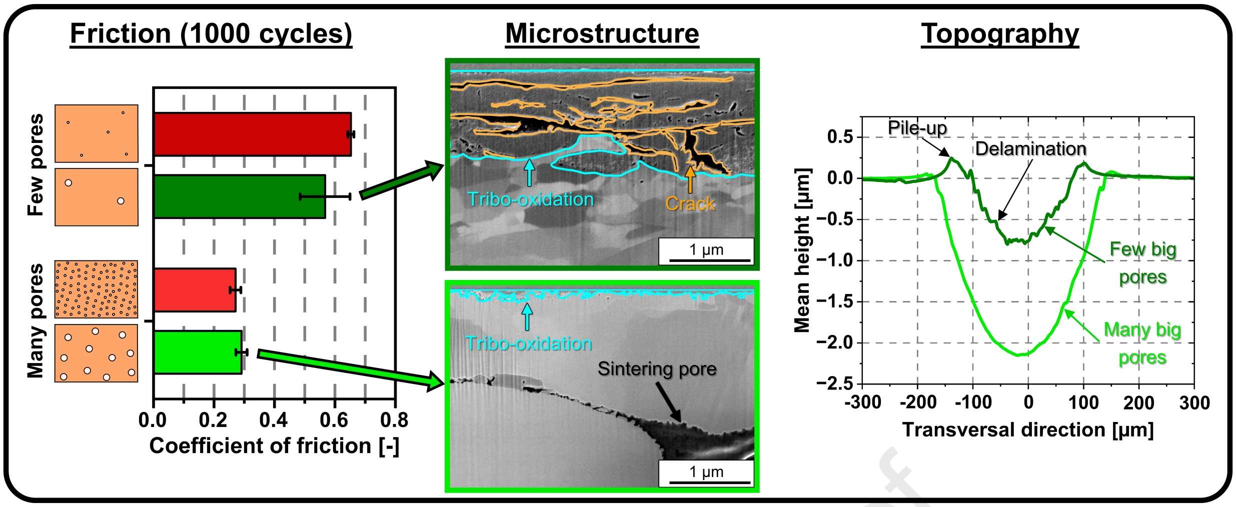

Friction (1000 cycles)
Microstructure
Topography
Few pores
Many pores
0.0
0.2
0.4
0.6
0.8
Coefficient of friction [-]
Tribo-oxidation
Crack
1 µm
Tribo-oxidation
Sintering pore
1 µm
Pile-up
Delamination
Few big pores
Many big pores
Mean height [µm]
0.5
0.0
−0.5
−1.0
−1.5
−2.0
−2.5
-300
-200
-100
0
100
200
300
Transversal direction [µm]

Porosity Matters: Exploring its Impact on the Unlubricated Tribological Behavior of Copper

*Roxane Lung[1], Karl Günter Schell[1], Christian Greiner[1]**

[1] Institute for Applied Materials (IAM), Karlsruhe Institute of Technology (KIT); Karlsruhe, 76131, Germany.

*: Corresponding author

E-Mail: R. Lung: roxane.lung@partner.kit.edu; K. G. Schell: guenter.schell@kit.edu; C. Greiner*: christian.greiner@kit.edu

Keywords: porosity, sintering, copper, tribology, friction, Cold Isostatic Pressing, density

Porosity is an inherent feature of manufacturing processes such as additive manufacturing or powder metallurgy, yet its systematic influence is still insufficiently understood. At the same time, improving the tribological properties of copper is crucial for its use in electronics, heat exchangers, and bearings. Since the tribological behavior of porous copper remains largely unexplored, this study systematically investigates the effects of pore size and porosity to fill this knowledge gap. Different specimen types were manufactured using Field Assisted Sintering Technology, with some undergoing an additional Cold Isostatic Pressing step. Tribological tests consisted of 1000 reciprocating cycles in a ball-on-flat tribometer. The results indicate that porosity, rather than pore size, has a dominant influence on friction behavior, with low relative density (~85%) specimens exhibiting a friction coefficient of about 0.3 and high-density (~96%) specimens around 0.6. In contrast to low-porosity samples, high-porosity specimens exhibit only minimal subsurface deformation, which results in limited tribo-oxidation and prevents surface delamination. Rather than forming pile-ups along the sides of the wear tracks, sintered particles are pressed into the sintering pores under tribological loading, resulting in 0.9-2 µm deeper and 100-200 µm wider

wear tracks. An additional densification of the specimens appears to exacerbate surface delamination, likely due to the increased dislocation density induced by the densification process.

1. Introduction

In manufacturing processes such as additive manufacturing with Laser Powder Bed Fusion or Selective Laser Sintering, and classical powder metallurgy techniques like Field Assisted Sintering Technology (FAST) or Isostatic Pressing, porosity can hardly be avoided [1–4]. Since pores typically lead to a deterioration of mechanical properties and also significantly affect the physical properties such as thermal and electrical conductivity, efforts are made to avoid them [5]. The necessity of improving tribological systems lies in the fact that 23% of global energy consumption is attributed to them [6]. Optimizing these systems, for example in machinery and vehicles, could lower overall energy consumption by up to 8%. For this, fundamental knowledge is essential. The presence of pores modifies the microstructure, impacting the material's tribological behavior, including wear rate and friction coefficient. Studies have shown that an increase in the porosity of stainless steel under dry sliding conditions can enhance wear resistance based on the assumption that the pores have to be filled with wear debris and plastic deformation during the first meters of sliding [7]. In contrast, Sinha et al. [8] reported that both the wear rate and coefficient of friction of pure aluminum and aluminum alloy 6061 rise with increasing porosity, attributing the higher wear rate to porosity-induced reductions in hardness and increased surface roughness, and the increased friction to greater asperity-asperity contact. In the case of lubricated contact, the results indicated that high porosity either increases or decreases friction, depending on the material pairing [9]. For combinations of same partners, such as Distaloy AQ+0.2% C or Astaloy CrA+1.8% Cr, both the coefficient of friction and wear increase with porosity. In contrast, for combinations of Distaloy AQ+0.2% C or Astaloy CrA+1.8% Cr with 16MnCr5, both friction and wear decrease as porosity increases. Recent findings by Chen et al. [10] demonstrate that nanopores in gold strengthen the material without reducing ductility by pinning dislocations. Thus, rather than being only disadvantageous, pores present opportunities worth exploring further. To date, no systematic investigation has examined how pores affect the tribological performance of copper under dry conditions, which further emphasizes the need for this investigation.

The tribological behavior of copper has already been investigated in several studies. According to Bowden and Tabor [11], friction force can be thought of in terms of an adhesion and a deformation component. In the real contact area between the surface of the specimen and the counterbody, junctions are formed due to adhesion and cold-welding, which require a specific force to be sheared off. Thus, the real contact area is proportional to the ratio of the total applied force to the indentation hardness of the softer material in the contact. The deformation factor arises from plowing, grooving or cracking of the softer surface by asperities on the harder one. The adhesion component of the friction coefficient can be calculated from the ratio of the shear strength to the indentation hardness or the yield pressure of the softer material [12].

A development of the microstructure has been observed in copper under tribological loading. During the first loading pass of a counterbody on a coarse-grained copper specimen, a dislocation trace line (DTL) forms at a depth of 100-150 nm, parallel to the surface, indicating a self-organization of dislocations [13]. With an increasing number of cycles, more dislocations accumulate within the DTL, leading to a rise in the misorientation angle until it most probably evolves into a small angle grain boundary (SAGB) [14]. At this stage, the DTL can be found at a depth of 200 nm. When exceeding 100 cycles, geometrically necessary dislocations accumulate to form cell walls that evolve into SAGBs and ultimately into subgrains, which are then gradually pushed deeper into the material [14, 15]. In highly strained copper, dislocation densities exceeding 10^{15} m^{-2} can be anticipated [16]. As stated by Huge and Hansen [17], the grain boundaries are aligned parallel to the surface, and at a strain of 12 MPa, grain sizes of about 10 nm form in the near-surface layers and coarsen with increasing depth from the surface. Furthermore, Argibay et al. [18] demonstrate that for pure metals, the low-friction regime (friction coefficient < 0.5) is linked to ultra-nanocrystalline surface films with grain sizes of 10-20 nm, which enable shear accommodation via grain boundary sliding. In contrast, in the high-friction regime (friction coefficient > 0.5), larger subsurface grains develop, and shear accommodation transitions to dislocation-dominated plasticity.

In addition to subsurface deformation, amorphous copper oxides form as islands preferentially at surface defects during the tribological loading in air [19]. Given that diffusion can occur faster at Cu_2O grain boundaries and at the copper-oxide interface than in the copper matrix, oxidation mainly takes place at the interface leading to the formation of semicircular clusters [19–21]. With increasing sliding cycles, the clusters expand further, leading not only to the nucleation of thermodynamically more stable Cu_2O nanocrystalline regions but also to the merging of the islands into a continuous oxide layer on the surface [19]. Since oxidation occurs before grain refinement, it progresses independently of it.

While numerous studies have already examined the behavior of dense copper under dry tribological loading in air, to our knowledge, no systematic investigations have been conducted on porous copper under tribological load. The amount and size of pores alter the microstructure and are therefore expected to influence the tribological properties. To assess this effect, the tribological behavior of copper specimens with varying pore densities and sizes is evaluated in the steady-state regime after 1000 sliding cycles, thereby complementing the long-term study of Lung et al. [22], who analyzed the tribological response up to 5000 cycles. The tribological behavior is analyzed under dry mild loading conditions, meaning low normal load and low sliding speed [14]. Copper under dry mild tribological conditions was selected because substantial fundamental knowledge has already been established. Thus, based on the insights already obtained on dense copper, the effect of the pores may be more clearly isolated and understood.

This study advances surface and interface science by revealing how porosity and pore size modify the contact mechanics and, consequently, the tribological behavior through changes in the coefficient of friction, subsurface deformation, tribo-oxidation and wear mechanisms. A key novel finding of this work is that porosity significantly lowers the coefficient of friction, while the influence of pore size remains comparatively minor. As porosity proves to be advantageous in dry tribological systems, post-processing of components to remove manufacturing-related porosity could be avoided, thereby saving additional energy [23]. Moreover, porous copper components could be increasingly relevant in lightweight, high-conductivity, and tribologically reliable applications by contributing to reduced energy and fuel consumption as well as lower emissions.

The primary objective of this study is to determine how porosity and pore size influence friction, wear mechanisms, and subsurface deformation, thereby offering new insights into the design of porous materials for tribological applications.

2. Experimental Section/Methods

2.1 Materials

In this investigation, two copper powders with a purity of 99.95%, provided by Inopowders S.A.S, Paris, France, were utilized. The remaining impurities comprised 17 ppm silver and other elements, each below 10 ppm. One powder exhibited a particle size distribution with a d90 of 20 µm, while the other had a d90 of 36 µm. To minimize oxidation, the powder was stored under argon atmosphere. The tribological tests were each conducted using a single-crystal sapphire sphere (SaphirwerkAG, Bruegg, Switzerland) as the counterbody with a diameter of 10 mm.

2.2 Sample Fabrication

In order to investigate the effect of the pores, different types of samples were fabricated according to Figure 1. The FAST process was carried out using a HP D 25/1 (FCT Systeme GmbH, Frankenblick, Germany). Various samples were produced, differing in the number and size of their pores. While the pore size was determined by the particle size of the powder used for sintering, the degree of porosity was defined by the force applied during the sintering process. Specimens with Few Small Pores (FSP) and Many Small Pores (MSP) were generated using the fine powder with a d90 of 20 µm. In contrast, specimens with Few Big Pores (FBP) and Many Big Pores (MBP) were produced using the coarse powder with a d90 of 36 µm. For this process, the powder was filled into a graphite die, 20 mm in diameter and lined with a graphite foil, to a height of 3.4 mm. Subsequently, the powder was manually pre-compacted with a force between 3 and 5 kN. During the FAST process, a pulsed current (25 ms pulse, 5 ms pause) was used. The samples were first subjected to a load of 5 kN while a vacuum (<1 mbar) was drawn for up to 3 min. This was followed by flooding the chamber with argon for 45 s, and then the vacuum was reapplied for an additional 1 min. Subsequently, the to-be specimens with few pores were loaded to 15.7 kN within 1.5 min, whereas those with many pores remained at 5 kN during this process step. Afterwards, they were heated to 450 °C at a maximum power of 21 kW, which corresponds to a heating rate of approximately 140 K min^{-1}. From 450 °C, a heating rate of 100 K min^{-1} was applied, allowing the specimens to be heated to 600 °C within an additional 1.5 min. All specimens were held at this maximum temperature for 2 min to ensure a comparable grain size across all sample types. Subsequently, the specimens were cooled down with a cooling rate of 100 K min^{-1}. Once 400 °C were reached, the specimens previously loaded to 15.7 kN were gradually relieved to 5 kN within 1 min, while the others remained at 5 kN. Finally, the chamber was vented, opened after 7 min, and the die was removed once it reached room temperature (~5 min later). To achieve a further reduction in porosity, and to investigate its influence on the tribological behavior, FSP and FBP samples were each produced in duplicate. In each case, one sample was only sintered, while the other underwent an additional Cold Isostatic Pressing (CIP) step, resulting in pressed specimens with few small pores (FSPC) and pressed specimens with few big pores (FBPC). During this process a KIP100E (Paul-Otto Weber GmbH, Remshalden, Germany) was used for 6 h at 400 MPa. As the pressing medium, Glykol PG46 (Dunze GmbH, Hamburg, Germany) was employed.

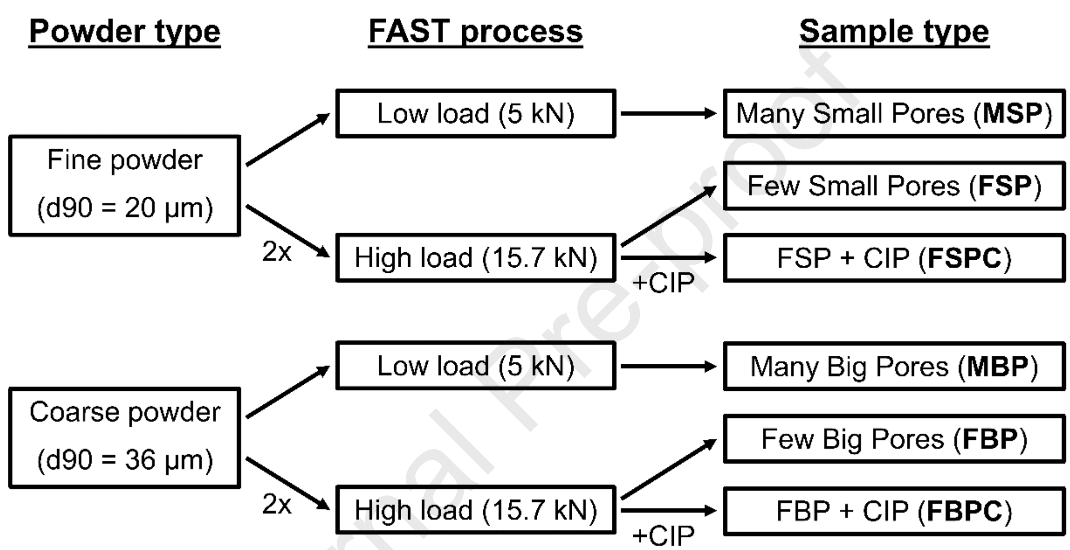

Figure 1. Overview of the key differences in the fabrication of the specimen types used in this study. After the field-assisted sintering technique (FAST), some samples underwent an additional cold-isostatic pressing (CIP) step.

2.3 Sample Preparation

After fabrication, the graphite foil on the surface of the copper specimens was ground off, and the samples were further ground with SiC grinding papers up to a grit size of 4000 using a Saphir 320, both from QATM GmbH, Mammelzen, Germany. Afterwards, the samples were polished with a LaboPol-30 and MD-Dur polishing cloths, both from Struers GmbH, Fellbach, Germany, using Mono 3 µm and Mono 1 µm diamond suspensions (Cloeren Technology GmbH, Wegberg, Germany) together with a lubricant consisting of 1000 ml distilled water, 10 g detergent, and 250 ml isopropanol. Subsequently, the specimens were vibropolished for 15 h using OP-U non-dry (Struers GmbH, Fellbach, Germany) with a VibroMet 2 (Buehler, Lake Bluff, Illinois, United

States) on a MicroCloth polishing cloth (Buehler ITW Test and Measurement GmbH, Leinfelden-Echterdingen, Germany) at an amplitude of 60%. The sample preparation concluded with a cleaning process using deionized water and detergent, followed by a final cleaning with isopropanol.

2.4 Tribological Testing

For the tribological experiments, the samples were mounted on a M-404.2DG precision linear stage (Physik Instrumente GmbH & Co. KG, Karlsruhe, Germany). The friction force was determined throughout the experiments using a piezoelectric, three-axis force sensor type Z16758 (Kistler Instrumente AG, Winterthur, Switzerland). The spheres were oriented with the help of a polarizer and a light source, so that their hexagonal close-packed basal plane was aligned parallel to the contact surface. During testing, a normal load of 2 N was applied to the spheres via a dead weight, and they were moved at a speed of 0.5 mm s^{-1} over a distance of 6 mm in the center of the specimens for 1000 reciprocating cycles. All experiments were carried out in air at room temperature and at a controlled relative humidity of 50%. Afterwards, the samples were immediately unloaded and stored in vacuum to avoid further oxidation. To verify reproducibility, all tests and analyses were repeated twice.

2.5 Subsurface Microstructure Characterization

After the tests, the specimens were systematically analyzed to identify and understand their tribological behavior and the differences between the samples. For this purpose, cross-sections were prepared with a focused ion beam (FIB) using DualBeam Helios NanoLab 650 from FEI, ThermoFisher Scientific, Waltham, Massachusetts, United States. Cross-sections were cut in the middle of the wear track, parallel to the sliding direction, as well as next to the wear track in the sample center, in order to examine the quantity and size of the pores using the software ImageJ (NIH, Bethesda, Maryland, United States). As the sintering pores exhibited a broad range of gray levels in the SEM images, they were manually colored with the software Inkscape (Inkscape Project, Boston, Massachusetts, United States) to ensure accurate identification in ImageJ. This preprocessing step enabled the thresholding procedure to reliably capture the entire pore area during image analysis. Before cutting the cross-section, two protective platinum layers were deposited on the sample surface, the first one with the electron and the second one with the ion beam. The imaging was performed in immersion mode with a current of 0.8 nA and an acceleration voltage of 2 kV.

2.6 Surface Characterization

The surface analysis was conducted using light microscopy images captured with an BX60 light microscope (Olympus, Tokyo, Japan), scanning electron microscopy (SEM) images using the FEI Helios 650, and optical surface profilometry images were obtained using the white light interferometer of the Plμ Neox (Sensofar, Barcelona, Spain). All images were taken in the center of the wear track. The height profiles of the individual wear tracks correspond to the mean value in the sliding direction over a distance of 1.2 mm. The grain orientation at the surface was measured using electron backscatter diffraction (EBSD). Scans were performed in the center of the specimen on a pre-tilted surface at 70° with a beam current of 13 nA and an acceleration voltage of 30 kV using a step size of 1 μm. To analyze the data, the Matlab toolbox MTEX was employed, generating color-coded maps based on the pole figures of the {100}, {110} and {111} directions [24].

2.7 Density Measurements

The overall densities of the different specimens were determined using the Archimedes method. A precision balance (type R160P-*D1, Sartorius AG, Göttingen, Germany) was used, and the thermometer was placed in the deionized water 2 h before the start of the experiment to obtain reliable measurements for the density of the water. To determine the density of the samples

$$\rho_S = m_{S(A)} / (m_{S(A)} - m_{S(W)}) \cdot (\rho_W - \rho_A) + \rho_A \qquad (1)$$

based on the densities of air $\rho_A = 0.0012$ g cm^{-3} and water ρ_W according to ISO 15212-1:1998, the specimens were weighed in air $m_{S(A)}$ and water $m_{S(W)}$ [25]. The measurements were repeated three times in both air and water, with the readings taken after 5 min. The mean value of the three measurements was used to determine the density. In order to calculate the relative density of the specimens, an absolute density of copper of 8.96 g cm^{-3} was assumed [26].

3. Results

3.1 Sample Analysis

For the pore analysis, both the overall density was measured using the Archimedes method, and the density in the center of the specimens was determined through image analysis of FIB cross-sections. It was observed that the porosity at the edges of the specimens is more pronounced than in the center, as seen in the SEM images in Figure 2 and Table 1. Thus, to ensure consistency, all tribological experiments as well as the analysis of the average pore sizes were conducted in the center of the specimens. Surface appearances and microstructures of the various sample types are shown in Figure A.1 and Figure A.2 in the supplementary information.

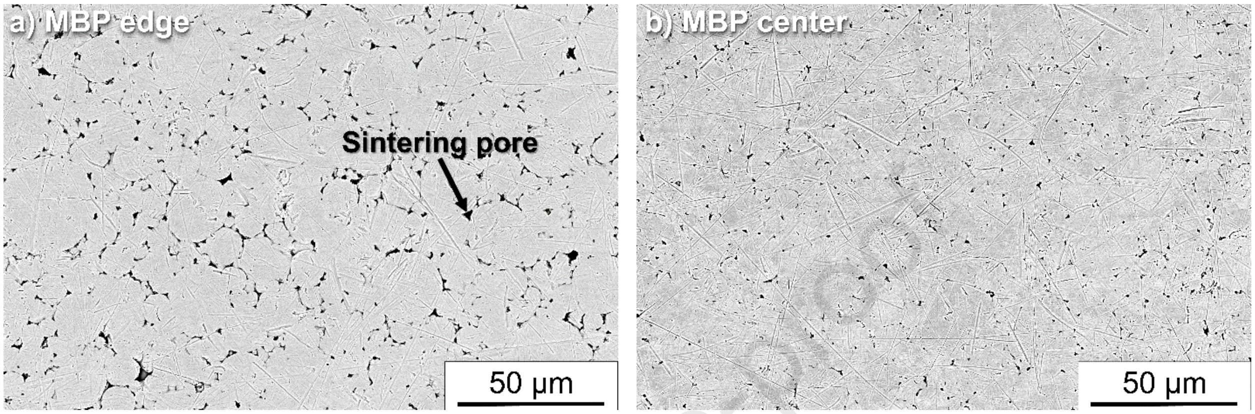

Figure 2. SEM images of a vibro-polished surface, which lays perpendicular to the current flow during the sintering process, taken a) at the edge and b) in the center of a Many Big Pores (MBP) specimen. It can be observed that the sintering pores are more pronounced at the edges of the specimens, which are enclosed by a graphite matrix.

Table 1. Comparison of the overall relative density of the different specimens, some of which were additionally Cold Isostatically Pressed (CIP), with the porosity measured in the center of the specimens.

Sample type	Relative density [%]	Porosity in the center [%]
Few Small Pores	96.7	1.6
Few Big pores	94.7	3.1
Many Small Pores	84.8	7.3
Many Big Pores	85.6	5.4
Few Small Pores + CIP	97.7	0.7
Few Big Pores + CIP	96.4	1.5

The samples produced with the finer powder exhibit smaller pore sizes, as shown in Figure 3, and a higher number of pores compared to those generated with the coarser powder. Using the finer powder, an average reduction in pore size of 1.9 μm^2 can be achieved for fewer sintering pores, while a reduction of 2.8 μm^2 can be attained for many sintering pores. Applying a force 10.7 kN lower during the FAST process results not only in an increase in pore size by 2.2 μm^2 for the finer powder and 3.1 μm^2 for the coarser powder, but also in an increase in porosity by 5.7% for the finer powder and 2.3% for the coarser powder. An additional CIP step leads to a reduction in pore size by 0.4 μm^2 and porosity by 0.8% for the samples generated with the finer powder, and a reduction in pore size by 1.7 μm^2 and porosity by 1.6% for the specimens made with the coarser powder.

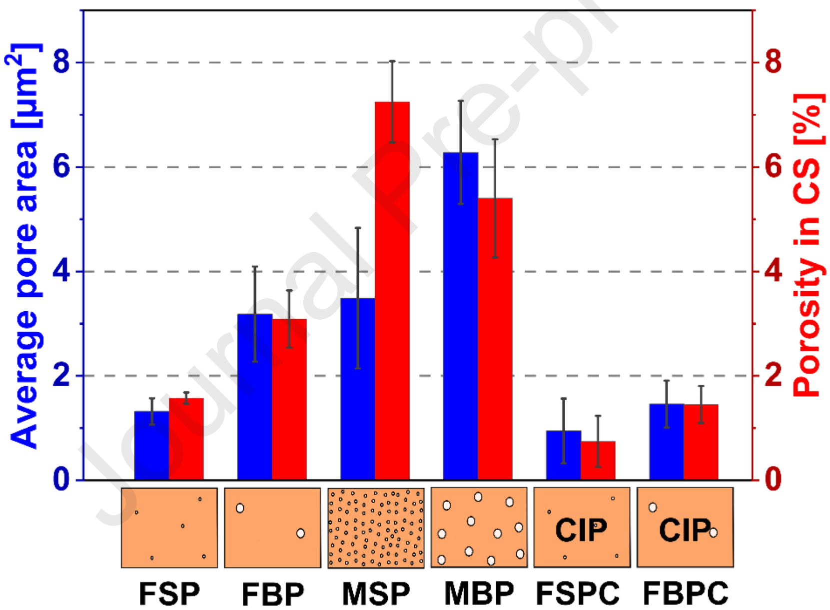

Figure 3. Average pore area and porosity measured in FIB cross-sections in the center of the different specimen types. The symbols indicate the number and size of pores and whether the sample was cold isostatically pressed (CIP). While the finer powder leads to a reduction in pore size and an increase in porosity, a lower force during the FAST process results in an increase in both pore size and porosity. The subsequent CIP-process reduces pore size and porosity.

In order to determine whether a possible anisotropy of the grain orientations needs to be considered in the tribological experiments and in the comparability of the results of the different specimen types, EBSD scans were performed. The pole figures in Figure 4 illustrate the grain orientation on the surface of the MBP specimen. They reveal that no significant anisotropy in grain orientation was present, since the maximum frequency of occurring clusters was 5.0%. Similarly, no significant anisotropy of grain orientation could be observed in FBP either, with a maximum cluster frequency of 3.5% visible in the orientation distribution functions in Figure A.3. Thus, sintering at both low and high forces did not cause substantial anisotropy in grain orientations. Consequently, no manufacturing-induced crystal orientation anisotropy needed to be considered, ruling out crystallographic orientation as a confounding variable and strengthening the conclusion that the observed effects are driven by the sintering pores.

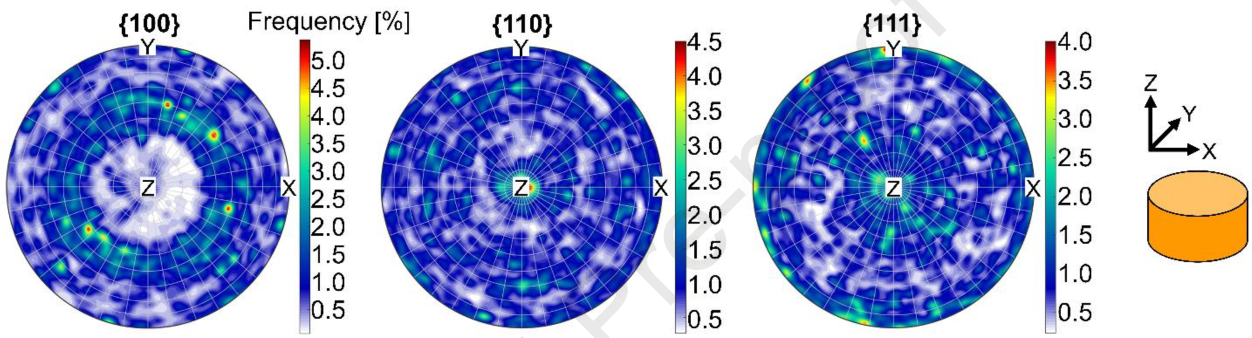

Figure 4. Pole figures showing the frequency of surface grain orientations for specimen MBP in the {100}, {110}, and {111} crystal orientations, with the X and Y directions lying within the plane of the specimen surface, and the Z direction oriented perpendicular to it.

After vibropolishing the surfaces of the different specimens, they exhibited varying roughness values. While FSP exhibited a *Sa* value of 0.05 µm and FBP a value of 0.06 µm, MSP had a *Sa* of 0.11 µm and MBP of 0.04 µm. The specimens that were additionally treated with a CIP step after the FAST process showed a *Sa* of 0.04 µm for both FSPC and FBPC.

The microhardness measurements of the vibropolished samples shown in Figure 5 indicate that FSP displayed an average hardness of 0.67 GPa with a standard deviation of 0.04 GPa, whereas FBP had an average hardness of 0.61 GPa with a standard deviation of 0.06 GPa. MSP and MBP exhibited lower hardness values, with MSP showing an average hardness of 0.48 GPa and a standard deviation of 0.01 GPa, and MBP showing an average hardness of 0.40 GPa and a standard deviation of 0.04 GPa. The CIP treatment carried out after the FAST process resulted in increased hardness values in the specimens with few pores. Consequently, FSPC showed an average hardness of 0.74 GPa with a standard deviation of 0.02 GPa, and FBPC had an average hardness of 0.92 GPa with a standard deviation of 0.08 GPa.

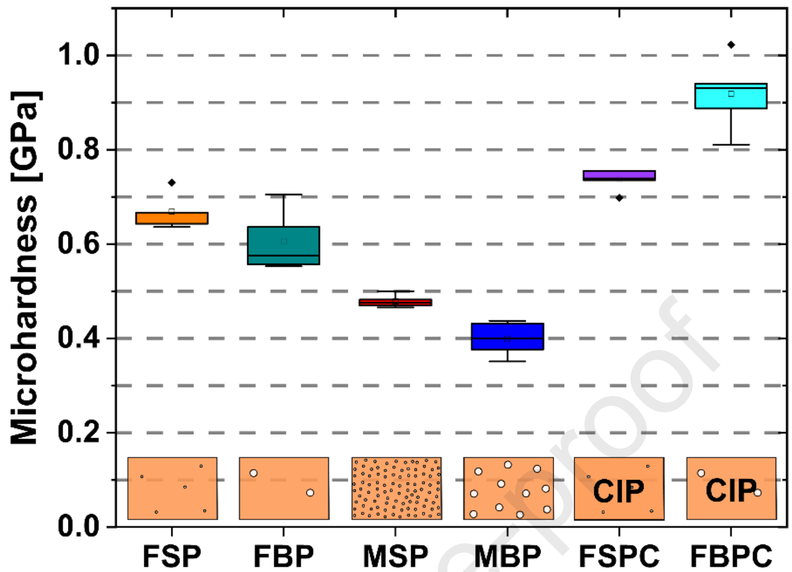

Figure 5. Microhardness measurements of the different samples. The box represents the interquartile range from the first to the third quartile, with the median as a line; whiskers show values within 1.5 times the interquartile range, outliers appear as diamonds and the mean as a square.

3.2 Tribological Behavior

The measured coefficient of friction over 1000 cycles, presented in Figure 6, shows a significant difference between specimens with low and high porosity. The evolution of the friction coefficient of specimens with low porosity increases significantly by 0.3 to 0.5 within the first 100-200 cycles, whereas it remains nearly constant in specimens with high porosity. While the friction coefficient of specimens with high porosity reaches a value of around 0.3 after 1000 cycles, it is at least twice as high in specimens with low porosity.

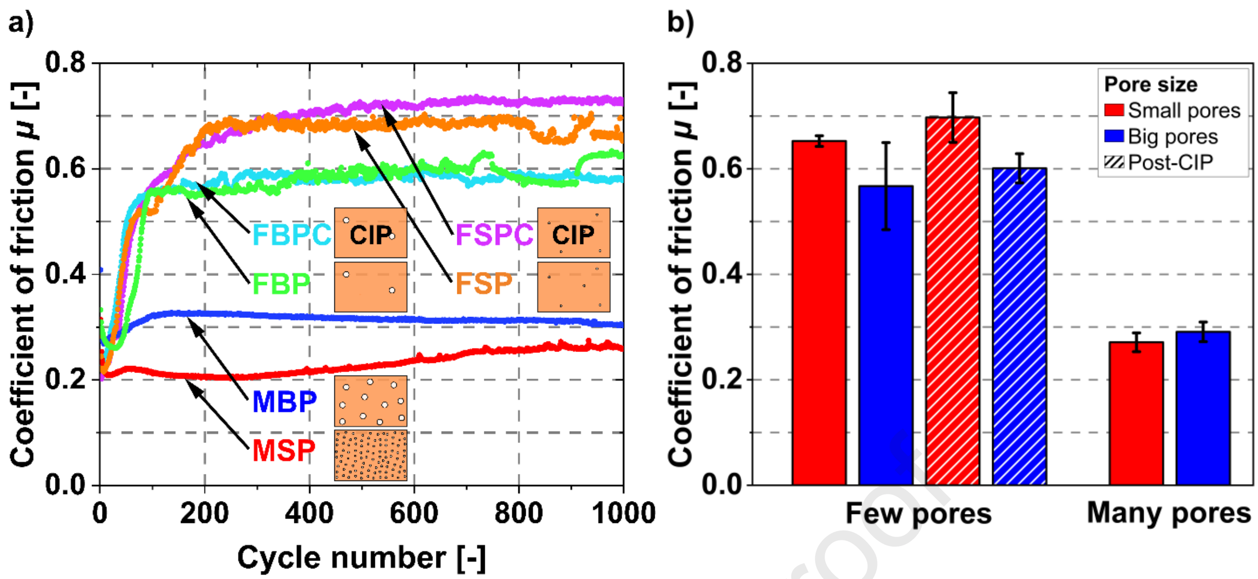

Figure 6. Friction coefficients of the different specimen types: a) over 1000 cycles and b) mean values with standard deviations at cycle 1000, with low-porosity specimens exhibiting approximately twice the friction coefficient of high-porosity specimens.

SEM analysis using secondary electron imaging, shown in Figure 7a to e, reveals that delamination occurred in the wear track of both the CIP specimens (Figure 7a and b) and the FBP specimens (Figure 7d). Neither the FSP specimens, nor those with high porosity, exhibit surface delamination due to the tribological tests. The zoomed-in backscattered electron (BSE) images of the MSP and MBP samples in Figure 7f and g reveal that sintered particles are still visible on the surface of the wear tracks even after 1000 cycles, indicating they were not deformed in sliding direction by the counterbody during the tribological experiments. Furthermore, there are significantly more grooves in the sliding direction on the low-porosity samples compared to the high-porosity ones, as exemplarily highlighted in Figure 7c.

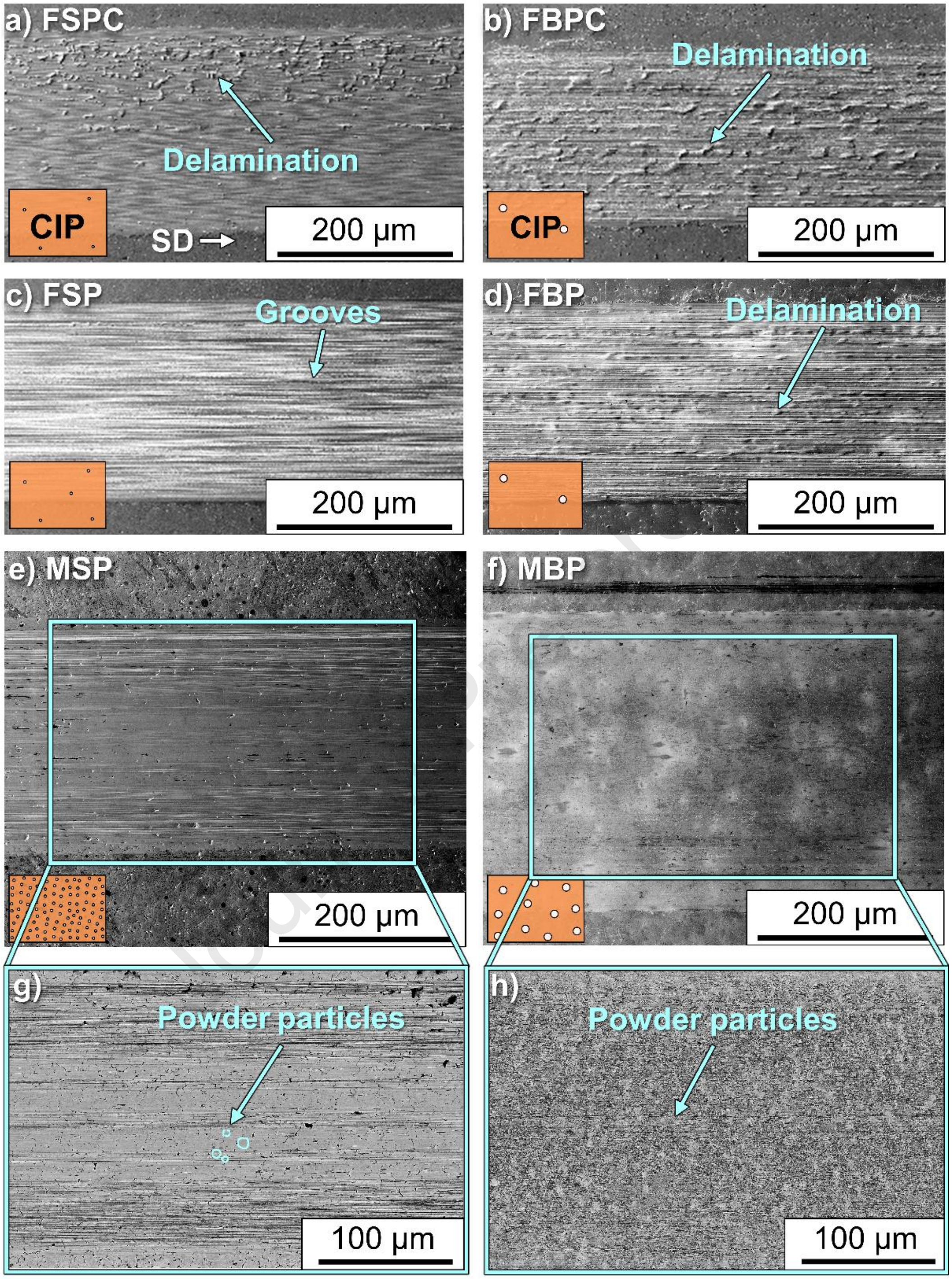

Figure 7. SEM images of the surfaces in the center of the wear track for various specimens. While secondary electron images are shown for a) FSPC, b) FBPC, c) FSP, d) FBP, e) MSP, and f) MBP, BSE images of the sections of specimens with high porosity are presented in g) and h). The sliding direction (SD) is valid for all images. Delamination can be observed on the surfaces of a), b), and d), while sintered particles, exemplarily highlighted in g), are visible in g) and h).

Figure 8 presents cross-sections in the sliding direction at the center of the wear tracks for the varying sample types. In all cross-sections, a dark gray zone can be seen directly beneath the surface (F1). While this zone is clearly visible in the cross-sections of specimens with low porosity (Figure 8a to d), it is barely present in specimens with a high porosity (Figure 8e and f). Among the low-porosity specimens, those with larger pores display a more pronounced dark gray area (Figure 8b and d) compared to those with smaller pores (Figure 8a and c). Additionally, black, elongated features (F2) appear in the dark gray zone in the FSPC, FBPC and FBP. In all cross-sections of the samples having a small number of sintering pores, black, circular features can be observed in the dark gray layer, which is shown exemplarily in Figure 8c along the interface between the dark and light gray areas.

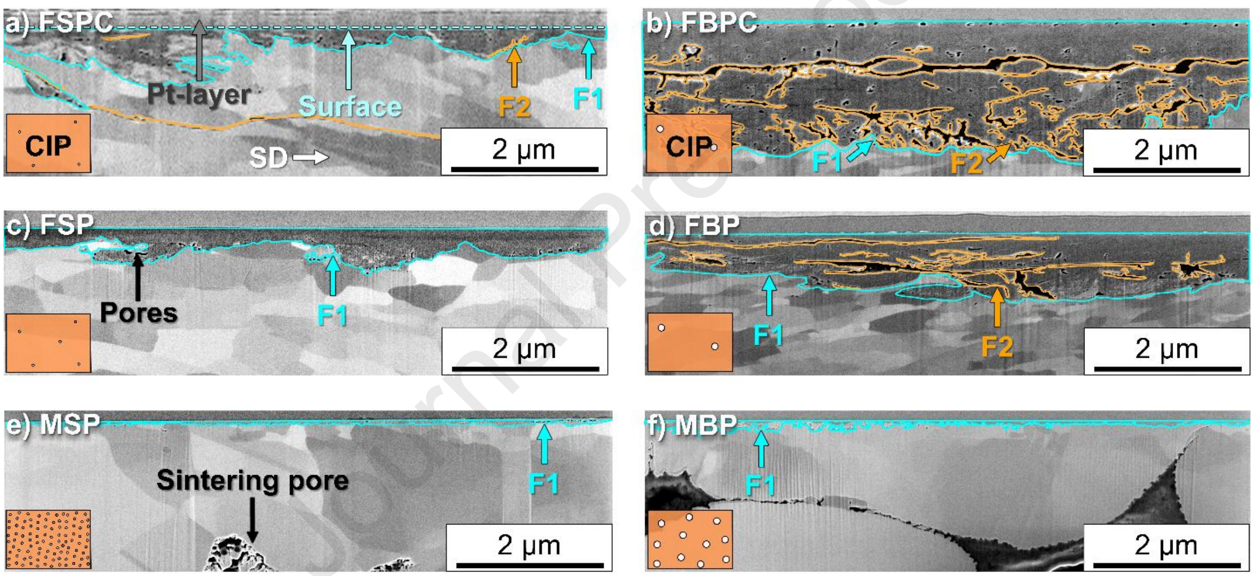

Figure 8. Cross-section images at the center of the wear track in sliding direction for a) FSPC, b) FBPC, c) FSP, d) FBP, e) MSP, and f) MBP. In a), the specimen surface is marked exemplarily beneath the platinum layer. The white arrow indicates the sliding direction (SD) in all images. In a), the specimen surface is marked exemplarily beneath the protective platinum layer. All cross-sections exhibit a dark gray zone beneath the surface (F1). Within F1, elongated features (F2) appear in a), b), and d). while black, circular features are observed particularly at the boundary of F1, as illustrated in c). In e) and f), sintering pores are visible beneath the sample surfaces, as highlighted in e).

In the light-microscope images, a discolored surface is visible along the wear track, as shown in Figure 9. High-porosity specimens exhibit a bluish-reddish surface, indicating the formation of

Cu_2O, while low-porosity ones appear darker [21]. In contrast to specimens with few sintering pores (Figure 9a to d), on the surfaces of samples with many sintering pores (Figure 9e and f), the colored area does not appear to be continuous, with individual copper-colored portions visible.

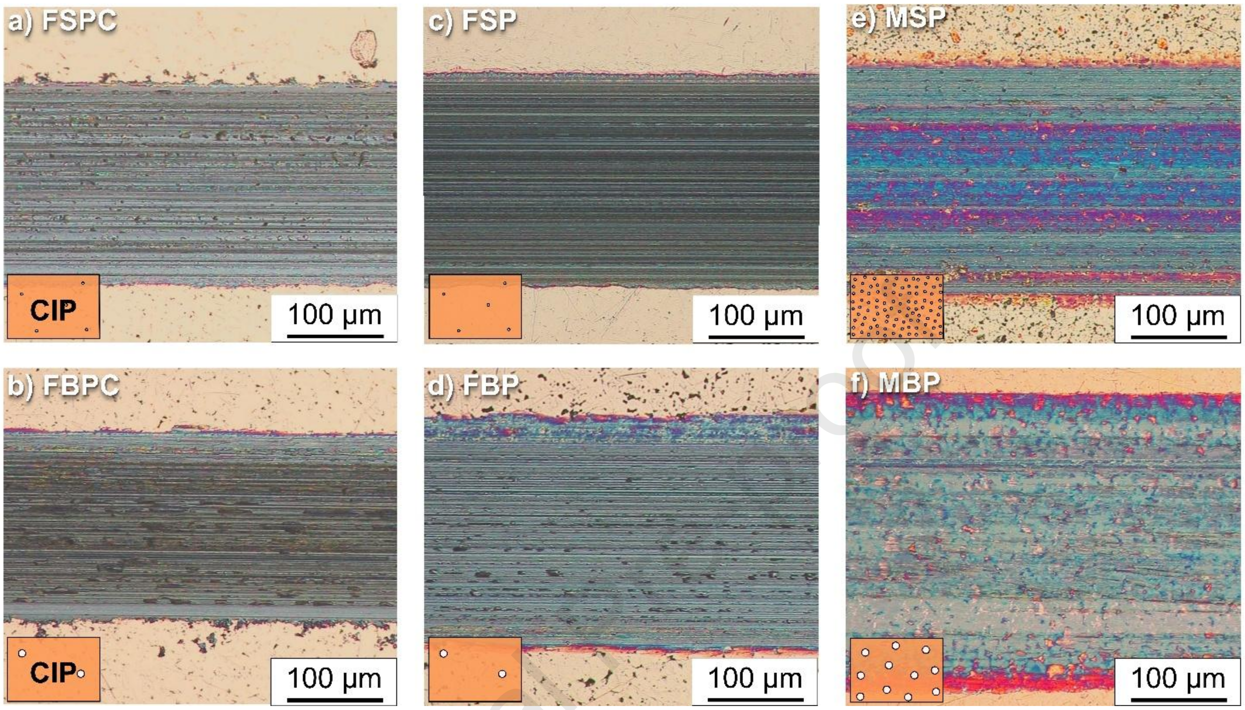

Figure 9. Light microscopy images of the surface in the center of the wear track of a) FSPC, b) FBPC, c) FSP, d) FBP, e) MSP, and f) MBP.

In addition to the tribologically induced dark gray zone, cross-sections in Figure 10 reveal a region beneath the surface of the various specimens where the grain sizes are smaller than those in the bulk material (DL). This zone extends deeper into the sample as the dark gray layer shown in Figure 8. For FSPC this area with smaller grain sizes is approximately 9.2 µm deep, about 8.2 µm for FBPC, around 10.8 µm for FSP, approximately 4.1 µm for FBP, and about 0.5 µm thick for MSP and MBP.

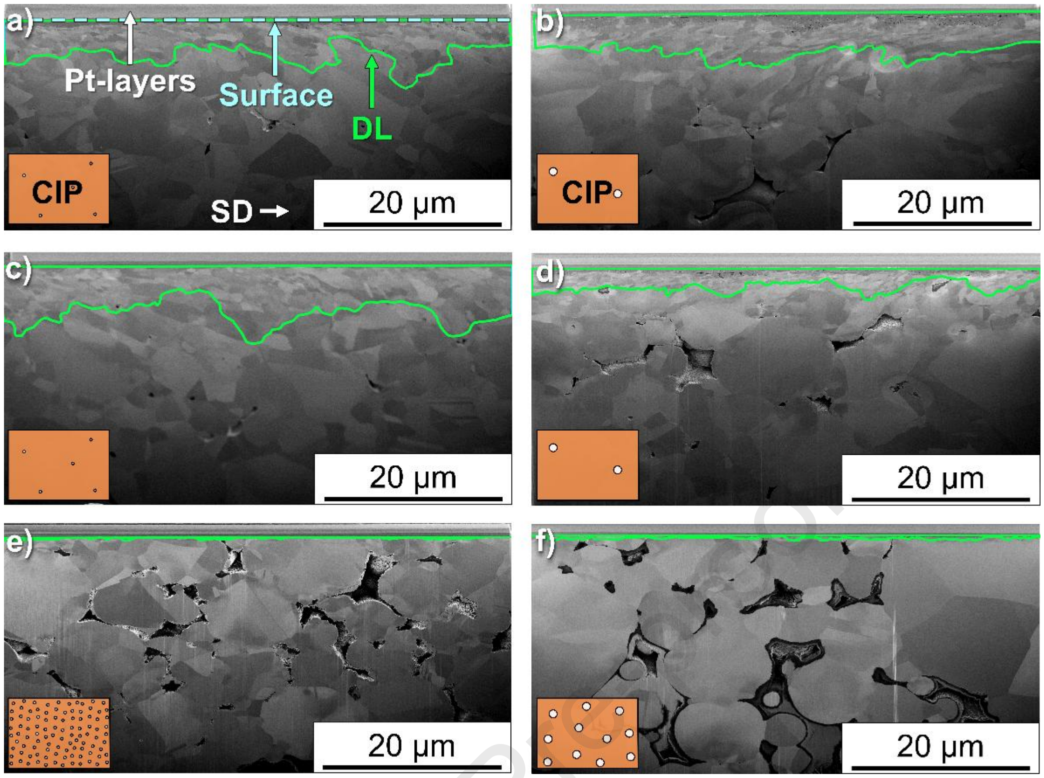

Figure 10. Cross-section images in sliding direction at the center of the wear track for a) FSPC, b) FBPC, c) FSP, d) FBP, e) MSP, and f) MBP, in which the subsurface deformation layers (DL) are marked in green, directly beneath the protective Pt-layers. The sliding direction (SD) is indicated in a). Specimens with many sintering pores in e) and f) exhibit a significantly smaller DL than those with few sintering pores in a) to d).

A difference in wear track profiles measured with a white light interferometer, and consequently in topographical deformation, is also noticeable between the samples with many and few sintering pores, as shown in Figure 11. While specimens with few sintering pores exhibit pile-ups at the edges of the wear track, those with many sintering pores are 0.9-2.0 µm deeper and 100-200 µm wider. Considering the wear track length of 6 mm, the projected cross-sectional areas of 275 μm^2 for MSP and 113 μm^2 for FSP in sliding direction correspond to an approximate topographical deformation volume of $1.65 \cdot 10^6$ μm^3 for MSP and $6.78 \cdot 10^5$ μm^3 for FSP. Additionally, it can be observed that the wear track of MBP is approximately 0.5 µm deeper than that of MSP.

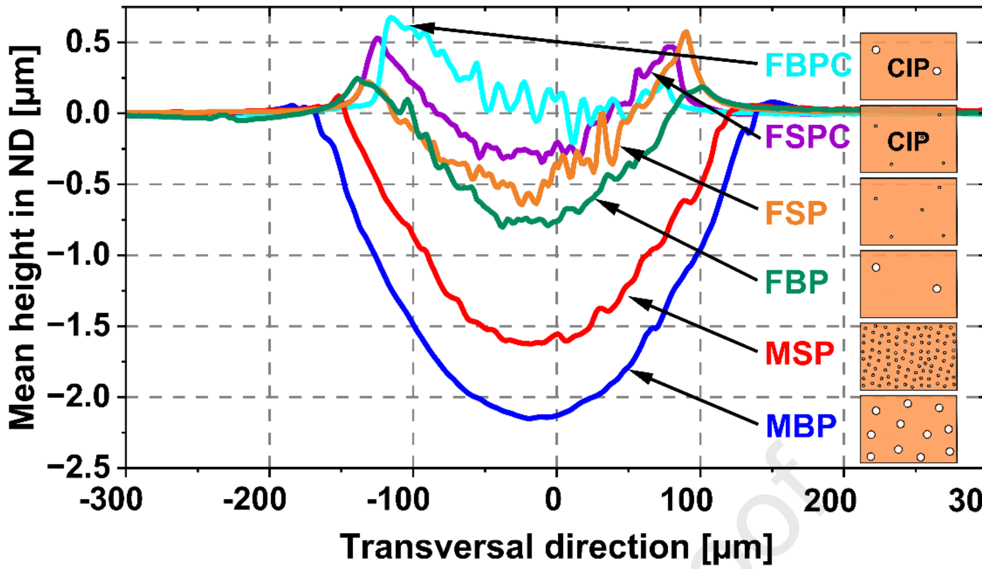

Figure 11. Average height profiles in normal direction (ND) of the wear track center for the various specimen types. The upper four curves correspond to low-porosity specimens, exhibiting lateral pile-ups, while the wear tracks of high-porosity samples, depicted in the lower two curves, are deeper and wider.

In light-microscope images of the sapphire spheres shown in Figure 12, which were used in tribological experiments on FSP and MSP samples, no significant difference in material transfer from the bulk to the sphere over the course of the tests can be observed. It is seen that the contact area of the sphere was larger in the MSP experiment, resulting in a wider wear track, in agreement with what was shown in Figure 11 for the wear track profiles. SEM imaging and EDS analysis shown in Figure A.4 indicate that, after 1000 cycles on an FSP specimen, both wear grooves and copper-containing wear debris are present on the sapphire sphere.

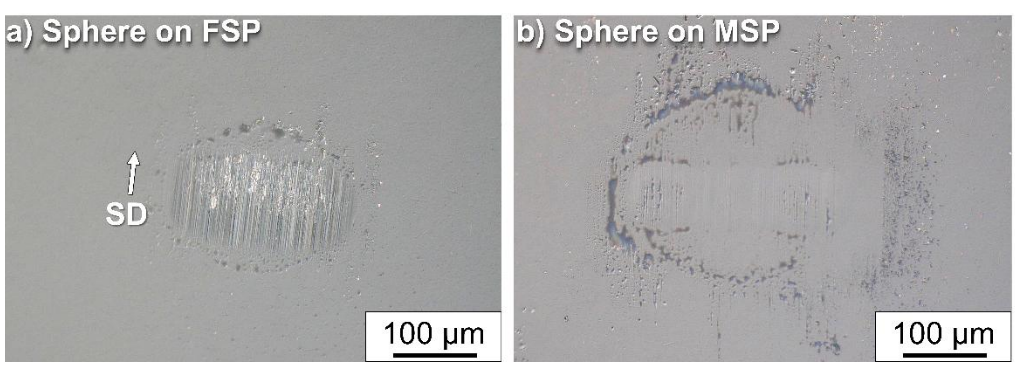

Figure 12. Light-microscope images of the sapphire spheres after tribological experiments with a) FSP and b) MSP. The sliding direction (SD) is indicated by the arrow.

4. Discussion

4.1 Influence of Porosity on Tribo-oxidation and Delamination

The leading question addressed in this study is whether pores have a beneficial or detrimental effect on the unlubricated tribological behavior of copper. In order to explore this, both the friction data collected during the experiments and the specimens are analyzed after the tribological experiments to gain insight into the underlying causes of the differences. As shown in Figure 6, it is evident that, unlike the sintering pore size and the additional CIP step, the number of sintering pores has a significant influence on the friction coefficient. The differences in friction coefficients identified in Figure 6 between specimens with many and few sintering pores can be attributed to variations in the evolution of the respective subsurface microstructures. This also includes surface delamination occurring during the tribological tests, as shown in Figure 7. Delamination, observed in the samples with elongated dark features (cracks) in Figure 8, is likely caused by these tribologically induced cracks. Since Rau et al. [27] identified similar features, it can be assumed that the small, round black areas are pores, and the dark gray area represents the tribo-oxidation layer. Both are formed during the tribological experiments. The large dark features in Figure 8e and f are process-induced sintering pores and were already present before the tribological tests. The tribo-oxidation layer, also visible in light-microscope images of the wear tracks for all specimen types in Figure 9, can be identified by the differently colored surface. During the tribological loading, Kirkendall pores form at the interface between oxide and copper due to the faster diffusion rate of copper ions compared to oxygen ions [27, 28]. With prolonged oxidation, pores also form along the diffusion paths [27]. As oxidation progresses, the oxidation layer grows deeper into the copper specimen, causing the interface between oxide and copper to shift inward. This may result in pores and cracks being visible at different depths after the 1000 cycles of tribological loading. These pores are highlighted at the oxide-copper interface in Figure 8c. Another reason for the delamination could be the higher hardness of the tribo-oxide, as Cu_2O has a hardness of 2.94 ± 0.02 GPa, while heat-treated, electropolished Cu-OFHC exhibits a hardness of 42 HV0.1, making the oxide more prone to crack initiation compared to the bulk material [19, 29]. In addition to the Kirkendall porosity, increased pore accumulation can occur due to dislocation pile-ups at harder phases, such as oxides, which can lead to surface delamination [30]. Alpas et al. [31] likewise reported that pores and consequently cracks can form in regions where the strain-hardening limit is exceeded. In the case of few sintering pores, specimens with large pores exhibit more pronounced tribo-oxidation, illustrated in Figure 8, and a higher degree of grain refinement beneath the surface compared to those with small sintering pores, as visible in Figure 10. This may result from a reduced real contact area between the specimen and the sapphire sphere, due to the larger pore volume and slightly higher porosity in the center of the specimen, as shown in Figure 2. This reduced contact area leads to increased stress concentration at the surface, resulting in a greater number of tribologically induced dislocations and grain boundaries, which both serve as diffusion paths for oxygen atoms [32]. Nevertheless, FSPC exhibits delamination and, consequently, more pronounced oxidation than FSP despite the small pores. Since the additional CIP of the sintered specimens results in reduced porosity, as shown in Figure 3, it can be assumed, according to James [33], that further deformation occurred within the microstructure, leading to an increased dislocation density. A higher initial dislocation density might thus accelerate the porosity formation induced by dislocation-pile-ups at the copper-oxide interface during the tribological loading and thus explain the crack formation in the tribo-oxide of FSPC. Similarly, Alpas et al. [31] observed that extensive plastic strains in the deformed zone promote failure.

In contrast to specimens with few sintering pores, those with many sintering pores exhibit only a small tribo-oxidation zone, as visible in Figure 8e and f. The reason for this might be the barely present subsurface deformation, as shown in Figure 10, which, in specimens with few sintering pores, acts as diffusion paths for oxygen atoms through generation and motion of dislocations [27]. The light microscopy images in Figure 9e and f reveal a reddish-blue shimmering oxide, characteristic of Cu_2O, which typically forms first during the oxidation of copper [34, 35, 21]. The oxide preferentially forms at surface defects as islands growing with advancing oxidation into semi-circular clusters into the bulk material [19]. However, as some copper-colored areas remain visible in Figure 9e and f, and as indicated by the shallow depth of the blue-highlighted tribo-oxide layer in the SEM images in Figure 8e and f, the tribo-oxide formed minimally and appears to have an island-like structure. Minimal oxidation and subsurface deformation in high-porosity specimens prevent crack formation and surface delamination (see Figure 7e and f). It was found that after 1000 passes, delamination and oxidation became the dominant mechanisms in controlling the coefficient of friction [36]. Thus, these differences between samples with many and few sintering pores are expected to have a significant impact on the differences in friction coefficients.

4.2 Subsurface Deformation and Contact Mechanics

In addition to the differences in the tribo-oxidation zones, there is also a significant difference in subsurface deformation between specimens with many and few sintering pores, as shown in Figure 10. It is evident that the subsurface deformation zone is significantly more pronounced in specimens with few sintering pores (Figure 10a to d) compared to those with many sintering pores (Figure 10e and f) which exhibits no significant tribologically caused subsurface deformation. The varying porosity levels at the surface influence the nominal Hertzian contact pressure. With a density of 86%, according to Buch and Goldschmidt [37], a reduction in the effective Young's modulus from 130 GPa to 100 GPa could be calculated [38]. This reduction is further supported by the correlation between decreasing hardness and a lower effective Young's modulus [39]. In line with this, the microhardness measurements in Figure 5 show that samples with high porosity exhibited lower surface microhardness values. Moreover, it can be expected that the samples with an additional CIP step exhibited a higher effective Young's modulus compared to those that were only sintered. Since the Poisson's ratio of sintered alumina decreases by 0.02 at a porosity of 22%, no change in the Poisson's ratio is assumed in the calculation of the Hertzian pressure of copper at a porosity of 14% [37]. Thus, a Poisson's ratio of 0.35 can be expected at room temperature for all the samples [38]. Considering that sapphire, according to Dobrovinskaya et al. [40], has a Young's modulus of 435 GPa and a Poisson's ratio of 0.27, a porosity-related reduction in Hertzian pressure of 74 MPa, from 581 MPa to 507 MPa, can be calculated [41]. A higher number of surface sintering pores is expected to result in a lower superposition of subsurface stresses at the contact edges, leading to regions of high stress being confined closer to the surface [42]. An investigation of the real contact area, comparing MBP with an overall density of 86% and FBP with 97%, reveals that the arc length of the wear track profile in Figure 11 reaches approximately 263 μm in MBP and is thus about 20 μm longer than in FBP, corresponding to an increase in real contact area of about 8%. This slightly larger real contact area suggests somewhat lower maximum surface stresses in MBP. In summary, both the reduced depth of stress distribution and especially the lower maximum surface stresses caused by a reduction in the effective Young's modulus together with the increased real contact area in specimens with high porosity are expected to contribute to their minimal subsurface deformation. Although an increase in real contact area would generally promote stronger adhesion, the significantly lower friction coefficient observed in high-porosity samples indicates that reduced subsurface deformation and oxidation-related effects dominate the friction behavior. The deformation-induced grain refinement beneath the surface of the specimens with few sintering pores is not caused by recrystallization phenomena, as the maximum temperature increase, according to Kuhlmann-Wilsdorf [43], is approximately 0.02 K. This can be determined for FSP using a friction coefficient of 0.7, a contact radius of the harder partner of 0.15 mm, a sliding distance of 6 mm, a microhardness of the softer partner of 670 MPa, a density of the softer partner $0.97 \cdot 8920$ kg m^{-3}, a specific heat capacity of the softer partner of 381 J kg^{-1} K^{-1}, and a volume of the copper cylinder of $2.827 \cdot 10^{-6}$ m^{3} [44]. Thus, the grain refinement can be attributed solely to the self-organization of dislocations, which initially arrange into wall-like structures, serving as the core process for the formation of subgrains and grain refinement [45, 46].

4.3 Wear Mechanism and Track Morphology

Notable differences in topographical deformation between the samples with many and few sintering pores are evident in Figure 11. In all wear tracks, plowing can be identified as the predominant wear mechanism. Plowing occurs when one surface is harder than the other, causing asperities on the harder surface to displace the softer material to a significant depth below the surface [47]. A certain amount of force is required to move the softer metal from the front of the slider. A significant variation in the plowing mechanism is apparent: while material in specimens with few sintering pores is pushed aside, forming pile-ups, sintered particles in specimens with many sintering pores are apparently pressed into the sintering pores, as schematically illustrated in Figure 13. This observation is supported by the fact that, in specimens with many sintering pores, there was no significant increase in material transfer to the sapphire spheres during the tribological experiments, as visible in Figure 12, nor was any debris found alongside the wear track. Moreover, it can be assumed that the sintered particles were not pulled out, as flattened sintered particles resulting from the preparation process are visible in the cross-sections, as shown in Figure 10. The sintered particles were most likely not partially worn away, as this would be accompanied by significant subsurface deformation and grooves at the surface, as observed in specimens with few sintering pores. As the wear track of MBP is deeper than that of MSP, it can be concluded that sintered particles are more easily pressed into the larger sintering pores. The differences in topographical deformation volume are due not only to the distinct plowing mechanisms but also to the oxidation-related volume increase in specimens with few sintering pores, making the difference appear larger [48].

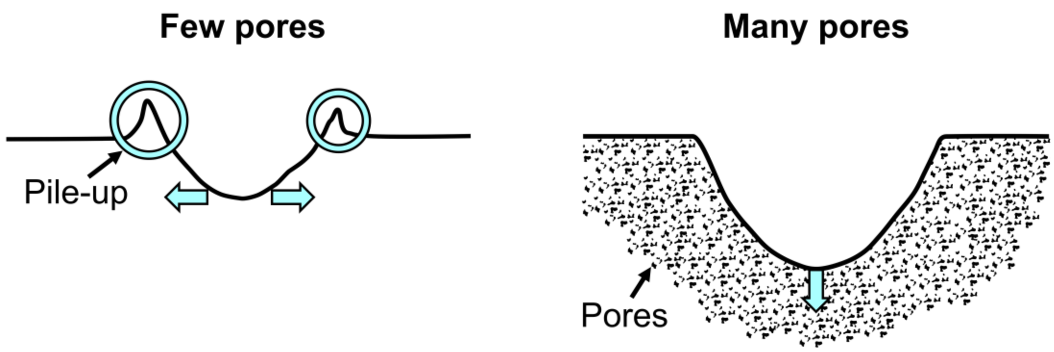

Figure 13. Schematic illustration of wear mechanisms at different porosity degrees: at low porosity, material is ploughed sideways, resulting in pile-ups along the wear track, whereas at high porosity, material is pressed into underlying pores. The directions of material displacement are indicated by blue arrows.

Both the initial microstructure and its evolution influence the coefficient of friction. Following Lafaye et al. [49], the plowing friction coefficient μ_P can be determined by means of the plowing friction force F_P and the normal force F_N. These can be calculated using the mean contact pressure ρ_a and the projected contact areas in sliding direction A_{SD} and in normal direction A_{ND} [50]. The plowing contribution in case of FSP can be calculated using the friction coefficient of 0.65 after 1000 cycles and

$$\mu_P = F_P / F_N = (\rho_a \cdot A_{SD}) / (\rho_a \cdot A_{ND}) = 0.0028 \quad (2)$$

based on the determination of A_{SD} = 113 µm^2 and A_{ND} = 39760 µm^2. With a proportion of 0.4%, the plowing contribution is significantly lower than the shearing contribution in the total friction coefficient. While the plowing contribution of 1.8% with μ_P = 0.0046 is higher in the case of MSP, based on A_{SD} = 275 µm^2 and A_{ND} = 59396 µm^2, it is still very small compared to the shear component. This is consistent with the theory of Bowden and Tabor, which states that for copper, the plowing term is very small [47]. Following Bowden et al. [11, 51], junctions form in the real contact area A_r between the sphere and the bulk, requiring a total force $S = A_r \cdot s$ to be sheared off, where s is the force per unit area necessary to shear the metallic junctions and acts tangentially to the interface. Since the real contact areas of the samples with many and few sintering pores are similar, and the plowing contribution is significantly smaller than the shearing contribution, the main influence on the difference in friction coefficients should be the force required to break the metallic junctions. However, since copper oxide is in contact with a sapphire sphere, the formed junctions are of ionic and covalent nature rather than metallic [52]. Accordingly, the present system will behave differently than in the Bowden and Tabor model and will not be based solely on mechanisms related to plasticity.

Beyond the macroscopic mechanical and oxidation behavior, the electronic state at the interface may also play a role. Given that plastic deformation affects the electron work function, porosity-dependent differences in plastic deformation could additionally affect the tribological behavior [53]. Specimens with many and few sintering pores, having the same sliding speed v during the tribological experiments and comparable contact areas resulting in similar nominal pressure p_N, exhibit differences in nominal friction power density

$$q_N = \mu \cdot p_N \cdot v \tag{3}$$

because of differing coefficients of friction μ, visible in Figure 6 [54]. The samples with many sintering pores exhibit a lower friction power density during the tribological experiments, which is evident from the lower nominal contact pressure, the lower friction coefficients in Figure 6 and the reduced energy dissipation, primarily due to the absence of subsurface deformation, crack formation, and minimal tribo-oxidation [55]. This results in significantly less plastic deformation beneath the surface. In contrast, plastic deformation is observed beneath the surface in the specimens with few sintering pores, and since the electron work function decreases with the onset of plastic deformation, different electron work functions are expected between the specimens with few and many sintering pores [53]. According to Li [56], adhesion in the metal-ceramic contact increases with decreasing electron work function. Consequently, a reduced electron work function in the specimens with few sintering pores, which is linked to a higher degree of plastic deformation, could lead to an increase in adhesion, which according to Bowden and Tabor is the primary component of the coefficient of friction. The influence of the electron state on the coefficient of friction has already been observed in other materials. For example, in ultra-nanocrystalline diamond, it is hypothesized that during the friction process, a rehybridization occurs, leading to a significant reduction in friction [53]. Thus, the different electron work functions in copper and its oxides for specimens with many and few sintering pores could also significantly influence the tribological properties.

Based on these results, the main question underlying this manuscript whether pores have a beneficial or detrimental effect on the tribological behavior of copper can be answered. As the sintered particles are pressed into the sintering pores, significant subsurface deformation does not occur, which results in minimal tribo-oxidation. Consequently, no pore agglomerates form beneath the surface that could lead to delamination. This lack of energy dissipation effects likely explains why the friction coefficient does not increase significantly within the first 100-200 cycles, as is the case with specimens containing few sintering pores, as visible in Figure 6. Consequently, sintering pores are beneficial for the unlubricated tribological behavior. Future studies could investigate how long the difference in friction coefficients between specimens with many and few sintering pores persists with increasing number of cycles. Additionally, the influence of the native oxidation layer on specimens with many sintering pores, as well as a closer examination of the friction coefficient increase after 50 cycles in the specimens with few sintering pores, could be explored in more detail. Furthermore, the tribological behavior of porous copper under lubricated contact should also be investigated.

4. Conclusion

This study demonstrates that a high porosity around 15%, rather than pore size, can reduce the dry sliding friction coefficient of copper by more than 50%, primarily by suppressing subsurface deformation and tribo-oxidation, indicating a beneficial tribological role for inherent porosity in manufacturing. To robustly establish this finding, the study employs a systematic sample design, in which pore size and porosity level were independently varied, combined with a multi-scale characterization before and after tribological testing to ensure reliable interpretation of the underlying mechanisms. Within this framework, specimens with different pore sizes and amounts of pores were sintered and then tribologically tested by moving a sapphire sphere with a normal force of 2 N and a speed of 0.5 mm s^{-1} over a distance of 6 mm in the center of the specimens for 1000 reciprocating cycles. Subsequently, both the wear tracks were analyzed using light microscopy and white light interferometry images, and the subsurface microstructures were examined through focused ion beam cross-sections and scanning electron microscopy. The densities of the specimens were investigated using the Archimedes method, and a possible grain orientation anisotropy at the surface was ruled out based on electron backscatter diffraction. The following main differences were identified:

i) Specimens with few sintering pores exhibit a thicker tribo-oxide layer and subsurface cracks compared to those with many sintering pores. This results in surface delamination, caused by the hardness of the thicker oxide layer, Kirkendall pore accumulation, and dislocation pile-ups at the oxide-copper interface. In specimens with many sintering pores the tribo-oxidation is minimal, as there is no significant subsurface deformation.

ii) An additional Cold Isostatic Pressing step introduces more dislocations, accelerating pile-up and crack formation. Larger sintering pores also result in greater grain refinement and oxidation due to increased surface stress concentration, creating more diffusion paths for oxygen. The small tribo-oxidation zone in specimens with many sintering pores is most likely due to minimal subsurface deformation, limiting diffusion paths for oxygen. The absence of these mechanisms contributes to the lower friction coefficient observed in specimens with many sintering pores.

iii)In specimens with high porosity, a reduction in Hertzian contact pressure from 581 MPa to 507 MPa caused by a decrease in the effective Young's modulus from 130 GPa to 100 GPa, together with lower maximum contact stresses resulting from an increased real contact area and high-stress regions confined closer to the surface, contribute to minimal subsurface deformation. In contrast, grain refinement in low-porosity specimens results from the self-organization of dislocations.

iv) Topographical deformation differs significantly: low-porosity specimens show material pile-ups, while high-porosity specimens exhibit sintered particles pressed into the sintering pores, resulting in reduced subsurface deformation. This interpretation is supported by the fact that specimens with many sintering pores show no significant increase in material transfer to the sapphire spheres during the tribological experiments, nor is there any additional debris found along the wear track. Furthermore, it can be assumed that the sintered particles are not pulled out, as preparation-induced flattened sintered particles are observed within the cross-sections. Additionally, the sintered particles are not partially worn away, as significant subsurface deformation would be visible, as observed in the specimens with few pores. Consequently, despite stronger topographical deformation, a higher wear volume cannot be assumed, as the deformation is largely accommodated by local particle displacement into pore space rather than material removal. The deeper wear track in the specimen with many big pores suggests easier particle embedding in larger pores. High-porosity specimens exhibit 0.9-2 μm deeper and 100-200 μm wider wear tracks. Differences in topographical deformation volume result from distinct plowing mechanisms and greater oxidation-induced volume increases in low-porosity specimens, amplifying the overall effect.

v) Since the specimens with few sintering pores exhibit a higher friction power density and thus more pronounced subsurface plastic deformation, which correlates with a reduction in the electron work function, this may increase adhesion and consequently friction.

These findings show that porosity in copper opens up new possibilities for reducing friction; at the very least in dry contacts. This could be of particular importance for additive manufacturing, such as laser powder bed fusion, as it offers a great flexibility in controlling porosity. In this context, further effects and their impact on the tribological behavior of copper could be explored, such as pore gradients, different types of pores like keyhole or under-melt pores, various pore shapes and their potential anisotropic effect on friction behavior. As the discussed mechanisms are likely not specific to copper, these promising results may also improve tribological performance in various other materials. Porous copper components may, for example, be applied in wind turbines as a dry-sliding grounding ring in the drivetrain, provided that the remaining electrical conductivity of $4.1 \cdot 10^{7}$ S m^{-1} at 15% porosity, despite a 32% reduction relative to bulk copper, is sufficient for reliable charge dissipation [57]. In such systems, continuous sliding contact occurs, while reduced density contributes to lower material consumption and reduced component mass, particularly for grounding rings mounted on shafts with diameters of several hundred millimeters [58]. Except for the study by Lung et al. [22], which supports the present findings, no systematic studies on porous copper under dry, mild tribological loading conditions have been published to date. This highlights a need for further investigations to substantiate the conclusions drawn in this study. Moreover, the present findings are limited to mild tribological loading conditions and an inert counter-body material. Therefore, future work should investigate the effect of porosity in metal–metal contacts as well as under more severe tribological conditions, such as higher normal loads or increased sliding speeds.

CRediT Authorship Contribution Statement

Roxane Lung: Writing – original draft, Visualization, Investigation, Data curation, Validation, Software, Formal analysis, Conceptualization. Karl Günter Schell: Investigation, Methodology, Resources, Writing – review & editing. Christian Greiner: Writing – review & editing, Supervision, Resources, Project administration, Funding acquisition.

Funding Sources

Funding of this work has partially been provided by the European Research Council under ERC Grant Agreement No. 771237 and by the German Research Foundation (DFG) under Project No. GR 4174/7.

Acknowledgements

The author is greatly indebted to Dr. Antje Dollmann and Dr. Yulong Li for the scientific discussions.

Data Availability

The raw data used for the analysis and evaluation of surfaces, subsurface microstructures and coefficients of friction, are published on KITopen DOI: 10.35097/q9q7nbnb7ggazf4m

Abbreviations

FAST, Field Assisted Sintering Technology; DTL, dislocation trace line; SAGB, small angle grain boundary; FSP, Few Small Pores; MSP, Many Small Pores; FBP, Few Big Pores; MBP, Many Big Pores; FSPC, cold isostatically pressed few small pores; FBPC, cold isostatically pressed few big pores; CIP, Cold Isostatic Pressing; FIB, focused ion beam; SEM, scanning electron microscopy; EBSD, electron backscatter diffraction; BSE, backscattered electron.

References

[1] F. Imani, A. Gaikwad, M. Montazeri, P. Rao, H. Yang, E. Reutzel, 2018. Process Mapping and In-Process Monitoring of Porosity in Laser Powder Bed Fusion Using Layerwise Optical Imaging. J. Manuf. Sci. Eng. 140, 101009. https://doi.org/10.1115/1.4040615.

[2] W. Wang, J. Ning, S.Y. Liang, Analytical prediction of keyhole porosity in laser powder bed fusion, Int. J. Adv. Manuf. Technol. 119 (2022) 6995–7002. https://doi.org/10.1007/s00170-021-08276-9.

[3] O. Guillon, J. Gonzalez-Julian, B. Dargatz, T. Kessel, G. Schierning, J. Räthel, M. Herrmann, Field-Assisted Sintering Technology/Spark Plasma Sintering: Mechanisms, Materials, and Technology Developments, Adv. Eng. Mater. 16 (2014) 830–849. https://doi.org/10.1002/adem.201300409.

[4] S.-J. L. Kang, 2020. What We Should Consider for Full Densification when Sintering. Materials. 13, 3578. https://doi.org/10.3390/ma13163578.

[5] S. Ji, Q. Gu, B. Xia, Porosity dependence of mechanical properties of solid materials, J. Mater. Sci. 41 (2006) 1757–1768. https://doi.org/10.1007/s10853-006-2871-9.

[6] K. Holmberg, A. Erdemir, Influence of tribology on global energy consumption, costs and emissions, Friction 5 (2017) 263–284. https://doi.org/10.1007/s40544-017-0183-5.

[7] F. Martin, C. García, Y. Blanco, Influence of residual porosity on the dry and lubricated sliding wear of a powder metallurgy austenitic stainless steel, Wear 328–329 (2015) 1–7. https://doi.org/10.1016/j.wear.2015.01.025.

[8] A. Sinha, Z. Farhat, 2015. Effect of Surface Porosity on Tribological Properties of Sintered Pure Al and Al 6061. Mater. Sci. Appl. 06, 549. https://doi.org/10.4236/msa.2015.66059.

[9] X. Li, U. Olofsson, A study on friction and wear reduction due to porosity in powder metallurgic gear materials, Tribol. Int. 110 (2017) 86–95. https://doi.org/10.1016/j.triboint.2017.02.008.

[10] J.-J. Chen, H. Xie, L.-Z. Liu, H. Guan, Z. You, L. Zou, H.-J. Jin, Strengthening gold with dispersed nanovoids, Science 385 (2024) 629–633. https://doi.org/10.1126/science.abo7579.

[11] F.P. Bowden, D. Tabor, 1966. Friction, lubrication and wear: a survey of work during the last decade. Br. J. Appl. Phys. 17, 1521. https://doi.org/10.1088/0508-3443/17/12/301.

[12] K.-H. Zum Gahr, Microstructure and Wear of Materials, Tribol. Ser. Vol. 10, Elsevier, Amsterdam New York, 1987.

[13] C. Greiner, Z. Liu, R. Schneider, L. Pastewka, P. Gumbsch, The origin of surface microstructure evolution in sliding friction, Scr. Mater. 153 (2018) 63–67. https://doi.org/10.1016/j.scriptamat.2018.04.048.

[14] C. Greiner, Z. Liu, L. Strassberger, P. Gumbsch, Sequence of Stages in the Microstructure Evolution in Copper under Mild Reciprocating Tribological Loading, ACS Appl. Mater. Interfaces 8 (2016) 15809–15819. https://doi.org/10.1021/acsami.6b04035.

[15] D.A. Rigney, J.E. Hammerberg, Unlubricated Sliding Behavior of Metals, MRS Bull. 23 (1998) 32–36. https://doi.org/10.1557/S0883769400030608.

[16] D.A. Rigney, M.G.S. Naylor, R. Divakar, L.K. Ives, Low energy dislocation structures caused by sliding and by particle impact, Mater. Sci. Eng. 81 (1986) 409–425. https://doi.org/10.1016/0025-5416(86)90279-X.

[17] D.A. Hughes, N. Hansen, 2001. Graded Nanostructures Produced by Sliding and Exhibiting Universal Behavior. Phys. Rev. Lett. 87, 135503. https://doi.org/10.1103/PhysRevLett.87.135503.

[18] N. Argibay, M. Chandross, S. Cheng, J.R. Michael, Linking microstructural evolution and macro-scale friction behavior in metals, J. Mater. Sci. 52 (2017) 2780–2799. https://doi.org/10.1007/s10853-016-0569-1.

[19] Z. Liu, C. Patzig, S. Selle, T. Höche, P. Gumbsch, C. Greiner, Stages in the tribologically-induced oxidation of high-purity copper, Scr. Mater. 153 (2018) 114–117. https://doi.org/10.1016/j.scriptamat.2018.05.008.

[20] Z. Liu, Microstructure evolution under tribological loading and its elementary mechanisms, Ph.D. Thesis, Karlsruhe Institute of Technology, Karlsruhe, 2018.

[21] S.-K. Lee, H.-C. Hsu, W.-H. Tuan, Oxidation Behavior of Copper at a Temperature below 300 °C and the Methodology for Passivation, Mater. Res. 19 (2016) 51–56. https://doi.org/10.1590/1980-5373-MR-2015-0139.

[22] R. Lung, K.G. Schell, C. Greiner, 2025. How Surface Treatment of Porous Copper Samples Dictates Dry Friction and Wear. Mater. Des. 258, 114584. https://doi.org/10.1016/j.matdes.2025.114584.

[23] X. Peng, L. Kong, J.Y.H. Fuh, H. Wang, 2021. A Review of Post-Processing Technologies in Additive Manufacturing. J. Manuf. Mater. Process. 5, 38. https://doi.org/10.3390/jmmp5020038.

[24] R. Hielscher, H. Schaeben, A novel pole figure inversion method: specification of the MTEX algorithm, J. Appl. Crystallogr. 41 (2008) 1024–1037. https://doi.org/10.1107/S0021889808030112.

[25] W.F. Koch, R.S. Davis, V.E. Bower, Direct Determination of Air Density in a Balance Through Artifacts Characterized in an Evacuated Weighing Chamber, J. Res. Natl. Bur. Stand. 83 (1978) 407–413. https://doi.org/10.6028/jres.083.026.

[26] N.A. Lange, Inorganic Compounds, in: J.A. Dean (Ed.), Lange's Handbook of Chemistry, 15th. ed., McGraw-Hill, New York, 1999, Ch. 3.

[27] J.S. Rau, S. Balachandran, R. Schneider, P. Gumbsch, B. Gault, C. Greiner, 2021. High diffusivity pathways govern massively enhanced oxidation during tribological sliding. Acta Mater. 221, 117353. https://doi.org/10.1016/j.actamat.2021.117353.

[28] J. Li, J.W. Mayer, E.G. Colgan, Oxidation and protection in copper and copper alloy thin films, J. Appl. Phys. 70 (1991) 2820–2827. https://doi.org/10.1063/1.349344.

[29] J.S. Lehmann, R. Schwaiger, M. Rinke, C. Greiner, 2021. How Tribo-Oxidation Alters the Tribological Properties of Copper and Its Oxides. Adv. Mater. Interfaces. 8, 2001673. https://doi.org/10.1002/admi.202001673.

[30] N.P. Suh, The delamination theory of wear, Wear 25 (1973) 111–124. https://doi.org/10.1016/0043-1648(73)90125-7.

[31] A.T. Alpas, H. Hu, J. Zhang, Plastic deformation and damage accumulation below the worn surfaces, Wear 162–164 (1993) 188–195. https://doi.org/10.1016/0043-1648(93)90500-L.

[32] D.M. Bailey, R.S. Sayles, Effect of Roughness and Sliding Friction on Contact Stresses, J. Tribol. 113 (1991) 729–738. https://doi.org/10.1115/1.2920686.

[33] P.J. James, Particle Deformation During Cold Isostatic Pressing of Metal Powders, Powder Metall. 20 (1977) 199–204. https://doi.org/10.1179/pom.1977.20.4.199.

[34] J.S. Rau, O. Schmidt, R. Schneider, R. Debastiani, C. Greiner, 2022. Three regimes in the tribo-oxidation of high purity copper at temperatures of up to 150 °C. Adv. Eng. Mater. 24 (11), 2200518. https://doi.org/10.1002/adem.202200518.

[35] C.G. Ribbing, A. Roos, Copper Oxides (Cu2O, CuO), in: E.D. Palik (Ed.), Handbook of Optical Constants of Solids, Academic Press, Burlington, 1997, pp. 875–882.

[36] H.M. Cao, X. Zhou, X.Y. Li, K. Lu, Friction mechanism in the running-in stage of copper: From plastic deformation to delamination and oxidation, Tribol. Int. 115 (2017) 3–7. https://doi.org/10.1016/j.triboint.2017.05.027.

[37] A. Buch, S. Goldschmidt, Influence of porosity on elastic moduli of sintered materials, Mater. Sci. Eng. 5 (1970) 111–118. https://doi.org/10.1016/0025-5416(70)90040-6.

[38] H.M. Ledbetter, E.R. Naimon, Elastic Properties of Metals and Alloys. II. Copper, J. Phys. Chem. Ref. Data 3 (1974) 897–935. https://doi.org/10.1063/1.3253150.

[39] J. Musil, F. Kunc, H. Zeman, H. Poláková, Relationships between hardness, Young's modulus and elastic recovery in hard nanocomposite coatings, Surf. Coat. Technol. 154 (2002) 304–313. https://doi.org/10.1016/S0257-8972(01)01714-5.

[40] E.R. Dobrovinskaya, L.A. Lytvynov, V. Pishchik, Properties of Sapphire, in: Sapphire; Springer US, Boston, 2009, pp. 55–176.

[41] I. Green, Poisson Ratio Effects and Critical Values in Spherical and Cylindrical Hertzian Contacts, Appl. Mech. Eng. 10.3 (2005).

[42] K. Komvopoulos, D.-H. Choi, Elastic Finite Element Analysis of Multi-Asperity Contacts, J. Tribol. 114 (1992) 823–831. https://doi.org/10.1115/1.2920955.

[43] D. Kuhlmann-Wilsdorf, Flash temperatures due to friction and Joule heat at asperity contacts, Wear 105 (1985) 187–198. https://doi.org/10.1016/0043-1648(85)90067-5.

[44] J. S. Rau, Mechanismen tribologisch-induzierter Oxidation in hochreinem Kupfer, Ph.D. Thesis, Karlsruhe Institute of Technology, Karlsruhe, 2021.

[45] C. Greiner, J. Gagel, P. Gumbsch, 2019. Solids Under Extreme Shear: Friction-Mediated Subsurface Structural Transformations. Adv. Mater. 31, 1806705. https://doi.org/10.1002/adma.201806705.

[46] B. Yao, Z. Han, Y.S. Li, N.R. Tao, K. Lu, Dry sliding tribological properties of nanostructured copper subjected to dynamic plastic deformation, Wear 271 (2011) 1609–1616. https://doi.org/10.1016/j.wear.2010.12.020.

[47] F.P. Bowden, D. Tabor, The Friction and Lubrication of Solids, Clarendon Press, Oxford, 2001.

[48] F.J. Wilkins, E.K. Rideal, T.M. Lowry, The kinetics of the oxidation of copper. Part I. The initial oxidation of copper at low pressures, Proc. R. Soc. Lond. A 128 (1930) 394–406. https://doi.org/10.1098/rspa.1930.0117.

[49] S. Lafaye, C. Gauthier, R. Schirrer, The ploughing friction: analytical model with elastic recovery for a conical tip with a blunted spherical extremity, Tribol. Lett. 21 (2006) 95–99. https://doi.org/10.1007/s11249-006-9018-7.

[50] C. Haug, Tribologisch induzierte Verformungsmechanismen und Reibung in Abhängigkeit von der Kristallorientierung in Kupfer, Ph.D. Thesis, Karlsruhe Institute of Technology, Karlsruhe, 2022.

[51] F.P. Bowden, A.J.W. Moore, D. Tabor, The Ploughing and Adhesion of Sliding Metals, J. Appl. Phys. 14 (1943) 80–91. https://doi.org/10.1063/1.1714954.

[52] P.A. Korzhavyi, B. Johansson, Literature review on the properties of cuprous oxide Cu2O and the process of copper oxidation, technical report SKB. https://skb.se/upload/publications/pdf/TR-11-08.pdf, 2011 (accessed 12 March 2025).

[53] A.L. Zharin, E.I. Fishbejn, N.A. Shipitsa, Effect of contact deformation upon surface electron work function, J. Frict. Wear 16 (1995) 66-78.

[54] M. Spreckels, Einfluss der Temperaturverteilung auf das tribologische Verhalten von Synchronisierungen, Ph.D. Thesis, University Hannover, Hannover, 2001.

[55] S. Ciraci, A. Buldum, Atomic-scale study of friction and energy dissipation, Wear 254 (2003) 911–916. https://doi.org/10.1016/S0043-1648(03)00246-1.

[56] Y. Li, Investigation of the relationship between the electron work function (EWF), adhesion and friction, Ph.D. Thesis, University of Alberta, Alberta, 2008.

[57] P. Grootenhuis, R.W. Powell, R.P. Tye, Thermal and Electrical Conductivity of Porous Metals made by Powder Metallurgy Methods, Proc. Phys. Soc. Section B 65 (1952), 502. https://doi.org/10.1088/0370-1301/65/7/305.

[58] Electro Static Technology, AEGIS Bearing Protection Handbook, Metric Version V3. https://www.bartlettbearing.com/wp-content/uploads/2021/06/Aegis-Handbook-edition-3.pdf, 2019 (accessed 29 April 2026).

Highlights

Porosity-induced drop in friction coefficient from 0.7 to 0.3

Porosity, rather than pore size, dominates the tribological behavior

Numerous pores reduce subsurface deformation and tribo-oxidation

High pore density prevents cracking and delamination under tribological loading

High porosity yields deeper (1-2 μm), wider (100-200 μm) wear tracks without pile-up

Declaration of interests

☒ The authors declare that they have no known competing financial interests or personal relationships that could have appeared to influence the work reported in this paper.

☐ The authors declare the following financial interests/personal relationships which may be considered as potential competing interests: